



Simultaneous nanostructure and heterojunction engineering of graphitic carbon nitride *via in situ* Ag doping for enhanced photoelectrochemical activity

S.W. Hu^a, L.W. Yang^{a,b,*}, Y. Tian^a, X.L. Wei^a, J.W. Ding^a, J.X. Zhong^a, P.K. Chu^{b,**}

^a Hunan Key Laboratory of Micro-Nano Energy Materials and Devices, Faculty of Materials, Optoelectronics and Physics, Xiangtan University, Hunan 411105, China

^b Department of Physics and Materials Science, City University of Hong Kong, Tat Chee Avenue, Kowloon, Hong Kong, China

ARTICLE INFO

Article history:

Received 1 July 2014

Received in revised form 6 August 2014

Accepted 16 August 2014

Available online 22 August 2014

Keywords:

Photocatalysis

Heterojunction

Nanosheets

Graphite-like carbon nitride

Mott–Schottky effect

ABSTRACT

A novel mesoporous ternary photocatalyst consisting of g-C₃N₄ nanosheets, metallic silver and MoS₂ nanosheets is prepared using AgNO₃ as a multifunctional modifier during thermal polymerization of melamine and few-layer MoS₂ in a simple one-pot process. The gas bubbles from AgNO₃ form an extra soft templates to *in situ* alter the polymerization behavior of melamine, creating thin g-C₃N₄ nanosheets and large porous structure that exhibit enhanced light absorption. The solution-based, soft-chemical synthesis enables homogeneous inclusion of metallic silver in the g-C₃N₄ nanosheets and high dispersibility of ultrathin MoS₂ nanosheets in the obtained nanocomposite. *In situ* coupling between metallic silver and g-C₃N₄ nanosheets produces nanoscale Mott–Schottky effect, provides an effective channel for charge separation and transfer, and tunes energy band of the latter. More importantly, modulated energy band of g-C₃N₄ nanosheets synergistically expedites the separation and transfer of photogenerated electron–hole pairs at the interface of two-dimensional g-C₃N₄/MoS₂ heterojunction. As a result, the ternary nanocomposite exhibits improved photoelectrochemical performance and photocatalytic activity under simulated sunlight irradiation compared with other reference materials. Our results provide new insights into the design and large-scale production of semiconductor photocatalyst.

© 2014 Elsevier B.V. All rights reserved.

1. Introduction

High-performance semiconductor photocatalysis is important to solar cells, water splitting, and environmental control [1–4]. Among various semiconductors, layered graphitic carbon nitride (g-C₃N₄, denoted as CN) analogous to graphite is especially attractive to conversion of solar energy to electrical or chemical energy because of its abundance, appropriate bandgap (~2.7 eV) and excellent chemical stability [5–12]. However, broader application of pristine CN is seriously hampered due to various factors including high recombination rate of photogenerated electron–hole pairs, low absorption coefficients, or poor catalytic activities [6,7].

Hence, extensive effort has been devoted to improve pristine CN with high activity and good working stability. Doping with metal [13–15] or nonmetal elements [11,16–19] has been proposed to resolve low photocatalytic efficiency of pristine CN, and binary heterojunction nanocomposite has recently emerged to be effective in high-performance CN-based photocatalysis [3,4,20,21]. In particular, two main types of CN-based heterojunction photocatalysis have been explored. One is nanocomposite prepared by physical mixing or *in situ* growth of another semiconductor with pristine CN [7,22–25]. For example, layered MoS₂ is considered one of the ideal candidates for the construction of semiconductor heterojunction with pristine CN due to suitable bandgap of about 1.8 eV [9,26,27]. The other is nanocomposite of pristine CN modified by highly conductive carbon materials such as carbon nanotubes as well as graphene and its derivatives [28–32]. Novel CN nanostructures such as mesoporous derivatives [9–11,33–36], nanotubes [37], nanorods [38] and nanosheets [12] endowing the materials with desired surface properties and morphologies, provide shortened pathway to promote charge migration and separation as well as mass diffusion/transfer during photoredox

* Corresponding author at: Hunan Key Laboratory of Micro-Nano Energy Materials and Devices, Faculty of Materials, Optoelectronics and Physics, Xiangtan University, Hunan 411105, China. Tel.: +86 73158292468.

** Corresponding author.

E-mail addresses: ylwxtu@xtu.edu.cn (L.W. Yang), paul.chu@cityu.edu.hk (P.K. Chu).

reactions. The coupled mediator of graphene or its derivatives acts as an electron transport “highway” or electron sink to facilitate the separation of photogenerated electron–hole pairs [2], whereas *p–n* heterojunction between pristine CN and another semiconductor functions as an electron separator to suppress the recombination of the photogenerated electron–hole pairs efficiently [3,4,39]. In addition, the coupled semiconductor with a smaller bandgap can extend light absorption range to improve light absorption performance. As expected, these CN-based nanocomposites exhibit better photocatalytic performance in splitting water and degrading pollutants than pristine counterparts. Despite recent progresses on many types of nanostructured CN-based binary heterojunction photocatalysis, practical application is still not satisfactory. In particular, the study of structural and electronic compatibility between pristine CN and co-catalysts has been limited so far. It is thus highly desirable, albeit challenging to develop new strategies of constructing novel CN-based nanocomposites to further enhance photocatalytic efficiency.

Coupling pristine CN with few-layer MoS₂ to form two-dimensional (2D) semiconductor heterojunction is an effective structure and electronic compatibility strategy to improve photo-conversion efficiency [9,10,40,41]. The 2D CN/MoS₂ heterojunction not only increases contact area for efficient charge transfer across the interface compared to zero-dimensional nanoparticles with only point contact, but also promote the separation of photo-generated electron–hole pairs due to shortened charge transport time and distance, thereby leading to the enhancement of overall photoconversion efficiency. Hou et al. reported that photocatalytic hydrogen evolution activity under visible-light irradiation was enhanced notably by producing thin layers of MoS₂ on mesoporous CN to form a 2D heterojunction [9]. Very recently, Chen et al. designed a 2D ternary nanojunction consisting of porous CN nanosheets, nitrogen-doped graphene, and layered MoS₂ [10]. This 2D ternary nanostructure exhibited a higher photocurrent density and photocatalytic activity than other reference materials under simulated sunlight irradiation since the introduced nitrogen-doped graphene interlayers worked as electron mediator for shuttling electrons and hole between the CN nanosheet and layered MoS₂ so that the separation of photogenerated electron–hole pairs was more effective. According to electrochemical analysis, the conduction-band and valence-band edge potentials of pristine CN have been determined at -1.13 and $+1.57$ eV, respectively [6,7,42]. The work functions of most noble metals are in between these two values, implying that the introduction of noble metal into pristine CN can produce a rectifying Mott–Schottky effect [42,43]. The formed Mott–Schottky effect extends the lifetime of charge carriers by enhancing the rate of electron–hole separation at noble metal–semiconductor interface. As a result, the catalytic performance of resulting hybrid catalyst is improved [44–48]. Hence, integrating 2D semiconductor heterojunction with Mott–Schottky effect is expected to be useful to construct high-performance CN-based photocatalysis.

Herein, we present the fabrication and characterization of mesoporous ternary nanocomposite consisting of CN nanosheets, metallic silver and MoS₂ nanosheets (denoted as CN–M–A). This ternary nanocomposite provides a broadening optical window for light harvesting and large contact area for fast interfacial charge separation and photoelectrochemical reactions. *In situ* coupling between metallic silver and CN nanosheets produces nanoscale Mott–Schottky effect, provides an effective channel for charge separation and transfer, and tunes energy band of the latter. More importantly, modulated energy band of CN nanosheets is helpful to the separation and transfer of photogenerated electron–hole pairs at the interface of 2D CN/MoS₂ heterojunction. As a result, the ternary nanocomposite is anticipated to exhibit good

photoelectrochemical and photocatalytic activities under visible light irradiation.

2. Experimental

2.1. Materials synthesis

The typical synthesis procedure for CN is *via* thermal condensation of melamine powder. In details, melamine powder (5 g) was put into an alumina crucible with a cover. Then it was heated with a rate of $5^{\circ}\text{C min}^{-1}$ to 550°C and kept this temperature for 4 h in air. The final yellow product was collected and ground with an agate mortar into powder. The ultrathin MoS₂ nanosheets with thickness about 5 nm (see Fig. S1) were prepared by hydrothermal intercalation and exfoliation method [49]. The procedure to prepare the CN–M–A ternary photocatalysis was as follows: 151 mg of AgNO₃ and 10 mg of MoS₂ ultrathin nanosheets were firstly dissolved in 5 mL deionized water with stirring. After being ultrasonicated for 30 min, melamine powder (5000 mg) was added to above suspension with stirring to make slurry. Finally, the slurry was thermally condensed with similar heating procedure and reaction time. With this method, CN–M–A ternary photocatalyst was obtained and ground with an agate mortar into powder for next characterization and testing. For comparison, binary photocatalysts of CN/Ag (denoted as CN–A) and CN/MoS₂ nanosheets (denoted as CN–M) were prepared using similar method without the presence of MoS₂ and AgNO₃, respectively.

2.2. Material characterization

The crystal structures of the synthesized samples were determined by powder X-ray diffraction (XRD, Rigaku, D/MAX 2500) using a copper K α radiation source ($\lambda = 0.154$ nm). X-ray photoelectron spectroscopy (XPS) measurements were performed by Axis Ultra instrument using an Al K α source (Kratos Analytical Ltd., UK). A binding energy of 284.8 eV for C 1s level was used as an internal. The morphology and microstructure of the samples were characterized using a field emission scanning electron microscopy (FESEM, Hitachi, S4800) with an energy dispersive spectroscopy (EDS) and transmission electron microscopy (TEM, JEOL 2100) equipped with selected area electron diffraction (SAED). N₂ adsorption–desorption measurements were conducted on a Nove 2200e analyzer. Raman spectra were recorded on a Renishaw InVia system with a laser operating at $\lambda = 785$ nm as excitation source. Fourier transform infrared (FTIR) spectra measurements were carried out on a FTS-3000 Fourier transform infrared spectrophotometer with KBr as the reference sample. Diffuse-reflectance UV–vis absorbance spectra of the samples were obtained using a UV–vis spectrophotometer (Shimadzu, UV-2550) with BaSO₄ as a reflectance standard. Photoluminescence (PL) spectra of the samples were obtained using a fluorescence spectrometer (Perkin Elmer, LS55) with an excitation wavelength of 350 nm. All measurements were performed at room temperature.

2.3. Photocatalytic tests

The photocatalytic activities of the samples were evaluated by the degradation of Rhodamine B (RhB) using a Xe lamp with AM 1.5G filter as simulated sunlight. A UV-cutoff filter ($\lambda > 400$ nm) was added to allow only visible light to pass through. The incident visible-light intensity was measured using a Radiometer (Model FZ-A, Photoelectric Instrument Factory, Beijing Normal University). The illumination intensity was kept at 100 mW cm^{-2} . The photocatalytic experiments were conducted at ambient temperature as follows: 40 mg of photocatalyst were added to 80 mL aqueous solution of 10 mg L^{-1} RhB. Before irradiation, the suspensions

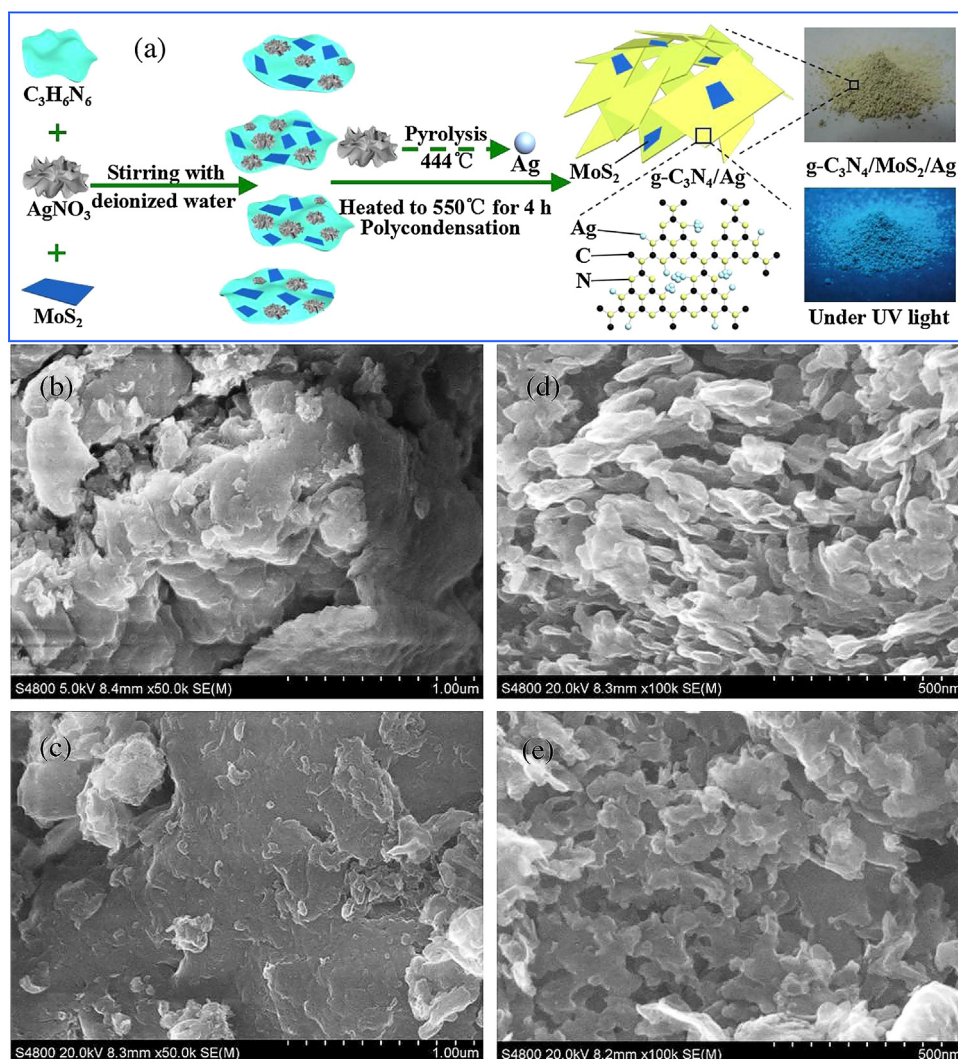


Fig. 1. (a) Schematic illustration of the synthesis process of the CN-M-A ternary photocatalyst. The right inset show the digital photographs acquired from CN-M-A under irradiation of white (upper) and UV-light (bottom); (b–e) FESEM images of CN, CN-M, CN-A and CN-M-A.

were stirred in the dark for 60 min to ensure the establishment of an adsorption–desorption equilibrium between the dye and the photocatalyst. At given irradiation time intervals of 20 min, 4 mL aliquots were withdrawn and then centrifuged to remove the catalyst. The degradation concentration of the RhB was determined using a UV–vis spectrophotometer (Shimadzu, UV-2550) at 554 nm. The photocatalytic stability of the CN-M-A ternary photocatalyst was evaluated by performing cycling runs on the degradation of RhB under similar conditions. After every 1 h of photodegradation, the separated photocatalysts were washed with deionized water for several times, and dried for next photodegradation.

2.4. Photoelectrochemical measurements

Photoelectrochemical measurements were performed on an electrochemical analyzer (CHI 660D) in a standard three-electrode configuration with a platinum wire as the counter electrode, Ag/AgCl (in saturated KCl) as a reference electrode, and Na₂SO₄ (0.5 M) aqueous solution as the electrolyte. The simulated sunlight was provided by a Xe lamp with an AM 1.5G filter and UV-cut-off filter ($\lambda > 400$ nm). The illumination power on the electrode surface was 100 mW cm^{−2}. The working electrodes were prepared on fluorine-doped tin oxide (FTO) conductor glass. Typically, the

powder (10 mg) was ultrasonicated in 1 mL of distilled water and 0.1 mL of Nafion D-520 dispersion (5%, w/w, in water and 1-propanol, Alfa Aesar) to disperse evenly to obtain a slurry. The slurry was spread on the FTO glass with the side protected by Scotch tape and dried at 120 °C for 1 h under vacuum condition. A copper wire was connected to the side of the working electrode using conductive tape and the uncoated parts of the electrode were isolated with epoxy resin. The transient photocurrent responses with time (*i*–*t* curve) of the working electrodes were measured at a 0.5 V bias potential during repeated ON/OFF illumination cycles. Cyclic voltammetry (CV) curves of the working electrodes were measured at the potential range of −1 to 0.6 V with scanning rate of 50 mV s^{−1}. Electrochemical impedance spectroscopy (EIS) measurements were carried out at open circuit potential by applying a perturbation voltage of 10 mV in a frequency range of 100 kHz to 10 mHz on a CHI660D electrochemical workstation.

3. Results and discussion

The synthetic procedure of CN-M-A ternary photocatalyst is illustrated in Fig. 1(a). Firstly, ultrathin MoS₂ nanosheets with a thickness of 5 nm (see Fig. S1) prepared by hydrothermal intercalation and exfoliation method are uniformly mixed with melamine in water *via* electrostatic interaction. After the introduction of AgNO₃

with weight ratio of 3%, CN-M-A mesoporous ternary nanocomposite is prepared by heating the composite of MoS₂ nanosheets, AgNO₃, and melamine at 550 °C in air for 4 h. During this process, the polycondensation of melamine to form CN is accompanied by *in situ* pyrolysis of AgNO₃ to metallic silver, N₂, O₂, and NO₂. The solution-based, soft-chemical synthesis enables homogeneous incorporation of metallic silver into the g-C₃N₄ matrix and high dispersibility of the ultrathin MoS₂ nanosheets in the final product. On account of preferential endothermic polycondensation of melamine, the formation of CN protects metallic silver and MoS₂ nanosheets from oxidation in air during the reaction at 550 °C. In particular, gas bubbles from the pyrolysis of AgNO₃ form an extra soft template [10,11], which *in situ* alters the polymerization behavior of melamine and favors the expansion of stacked CN layers to produce thin layers of nanosheets and large porous structure. As shown on the right side of Fig. 1(a), under UV light illumination, gray-yellow CN-M-A ternary nanocomposite has stable blue emission, which is visible to the naked eye and similar to that of pristine CN (see Fig. S2). The results imply that the addition of MoS₂ nanosheets and AgNO₃ has no obvious effect on original graphitic C–N motif and PL property of pristine CN.

Fig. 1(b) shows typical SEM image of the prepared CN, exhibiting bulk morphology. No obvious difference of morphology can be observed from CN-M as shown in Fig. 1(c). Fig. 1(d) depicts typical SEM image of CN-A, showing a loose and porous structure. The results confirm that the gas bubbles produced from the pyrolysis of AgNO₃ plays an important role in the morphological evolution of final product. Fig. 1(e) displays typical SEM image of CN-M-A. A porous structure is also observed, but the product looks more compact. Owing to the similarity of 2D structure, the CN is likely sandwiched between MoS₂ nanosheets through polymerization of melamine pre-adsorbed on the latter, so that CN-M-A possesses a more compact sheet-on-sheet structure. No bulk-phase separation between CN and MoS₂ nanosheets is observed by SEM and EDS, indicating that layered MoS₂ nanosheets are highly dispersed in CN-M-A. The textural properties of all samples are characterized by nitrogen gas porosimetry to evaluate specific surface area and porous structure. The nitrogen adsorption–desorption isotherms in Fig. 2(a) show type IV isotherms with distinct H₃ hysteresis loops, which is characteristic of mesoporous materials. Based on Barrett–Joyner–Halenda model, all of samples possess similar pore size in the range of 2–150 nm and main pore size is 3.7 nm (see Fig. 2(b)). The formation of pore with size of 3.7 nm is attributed to released gas bubble that serves as a soft template during polymerization of melamine [10]. The larger pores are produced due to the platelet-like morphology of CN and MoS₂. The BET specific surface areas are calculated to be 13.83 m² g^{−1}, 15.2 m² g^{−1}, and 22.7 m² g^{−1} for CN, CN-M, and CN-A, respectively. As expected, a marked increase in specific surface area is observed when the AgNO₃ is introduced to produce extra gas bubbles to expand stacked CN layers. The larger surface area observed from CN-A is due to more pores at 3.7 nm and pores in the range from 5 to 50 nm (see Fig. 2(b)). Although simultaneous introduction of MoS₂ nanosheets and AgNO₃ decreases the total specific surface area, a remarkable value of 20.4 m² g^{−1} is still observed from CN-M-A. With a large specific surface area, hybrid photocatalyst has great promise in not only facilitating mass transfer, but also offering sufficient interfacial area for adsorbing molecules and photoelectrochemical reactions to ultimately improve photocatalytic performance.

The microstructures of the prepared photocatalysts are then examined by TEM and high-resolution TEM (HRTEM) observations. The TEM image in Fig. S3a shows that the CN monolith is composed of large sheets without large porous structure. Fig. S3b displays typical TEM image of CN-M, revealing that the layered CN is on the surface of single MoS₂ nanosheet to form a close

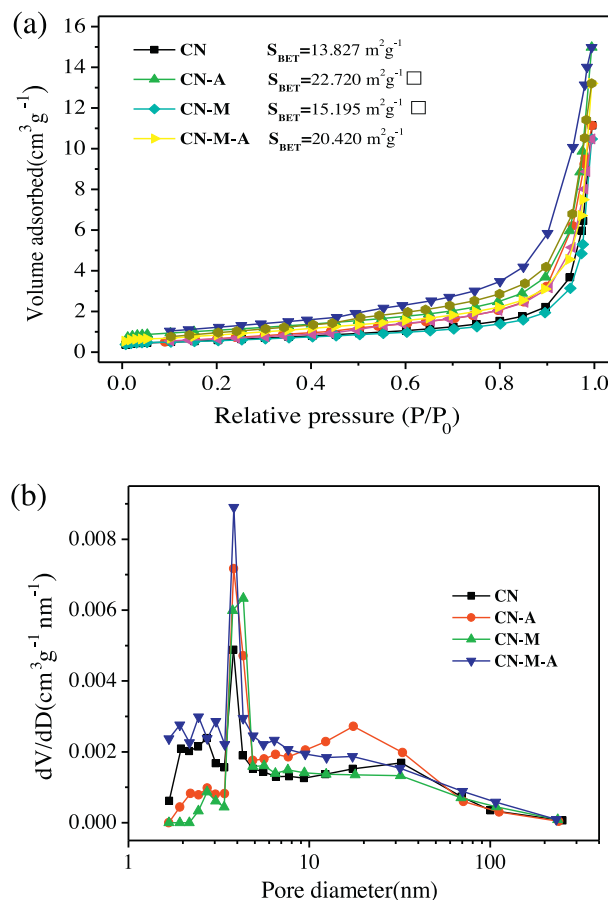


Fig. 2. (a) Nitrogen adsorption–desorption isotherms and (b) corresponding pore size distribution curves obtained from CN, CN-A, CN-M and CN-M-A.

2D g-C₃N₄/MoS₂ contact. The sharp SAED patterns (see the inset of Fig. S3b) indicate that MoS₂ nanosheets with high crystallinity keep unchanged after thermal treatment at 550 °C, confirming the protective effect against oxidation during polycondensation of melamine. Fig. 3(a) and (b) depict typical TEM images of CN-A. A typical porous morphology consisting of small thin nanosheets with wrinkles and irregular shape can be observed. The HRTEM image and SAED patterns (see Fig. 3c and its inset) indicate that CN-A is amorphous. Fig. 3(d) and (e) displays typical TEM images of the prepared CN-M-A, exhibiting a porous morphology with small thin nanosheets, which is similar to that of CN-A. These small thin nanosheets are highly desirable in photochemical applications because the reduced thickness shortens the transport distance of charge from the bulk to the surface, whereby the photoredox reaction takes place [11]. As shown in Fig. 3f, a single MoS₂ nanosheet embedded in the CN-M-A host can be observed. The SEAD patterns and HRTEM image (see Fig. 3f) confirm high crystallinity of layered MoS₂ nanosheets. The visible set of lattice fringes with a lattice spacing of 0.22 nm is characteristic of the (1 0 3) lattice plane of hexagonal MoS₂ (PDF No. 37-1492). No big silver particles appear on the surface of CN-A and CN-M-A, however a few black spots with the size of less than 1 nm as marked by circles can be observed in HRTEM image. These black spots likely originate from very small and highly dispersed silver, which is similar with that reported by Bu et al. [46]. Nevertheless, the presence of metallic Ag can be undoubtedly discerned by EDS, Raman spectra, CV and XPS to be discussed later.

The chemical composition and structural properties of CN-M-A are evaluated by EDS, CV, and Raman spectra. The EDS analysis and corresponding element mappings (see Fig. 4 and Fig. S4) detects

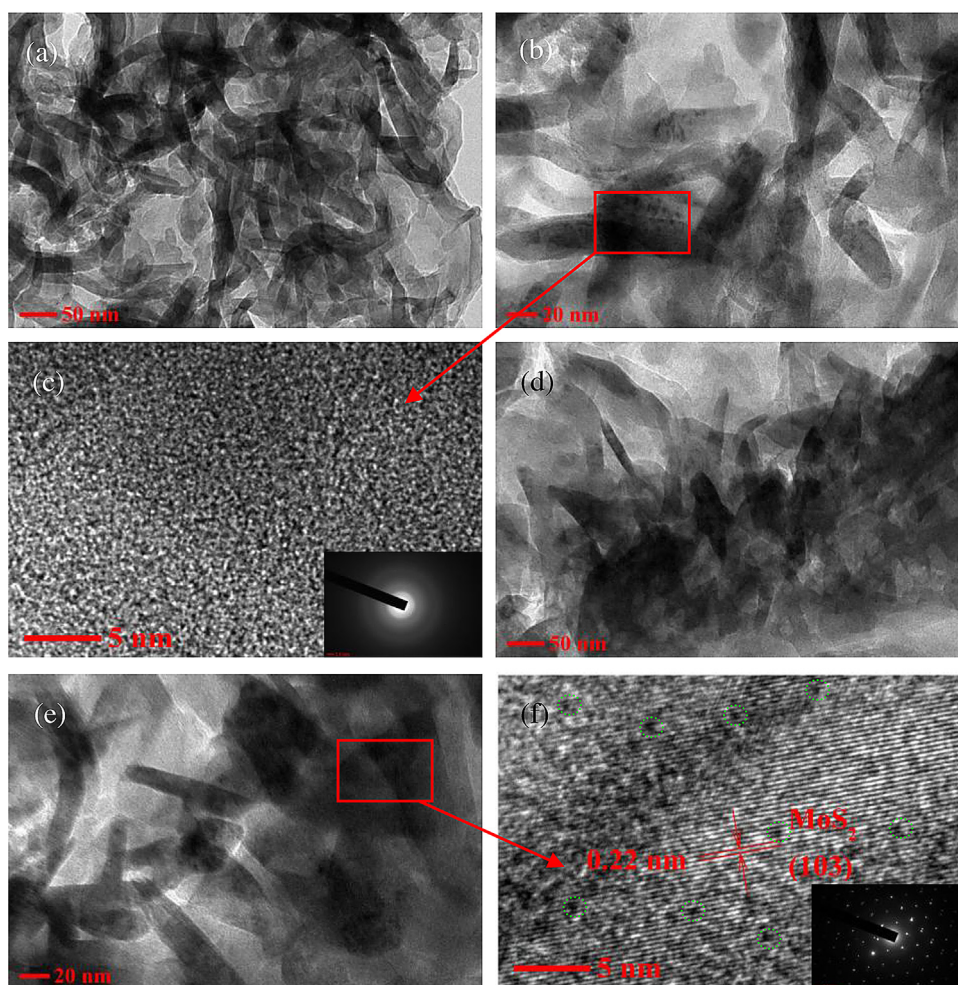


Fig. 3. (a–c) Typical TEM image, HRTEM image and SAED patterns of CN-A; (d) and (e) typical TEM images of CN-M-A. (f) HRTEM image and SAED patterns of the marked area in (e).

the presence of Ag in addition to C, N, Mo, and S. Quantitative EDS reveals that the weight ratio of Ag is about 2.7%, which is close to nominal amount added during the synthesis. Particularly, the element mappings of Ag shown Fig. 4b indicate Ag is uniformly distributed in CN nanosheets. Fig. 5(a) shows CV curves of the photoelectrodes composed of different photocatalysts. No significant redox peaks are observed from the CV curves of CN and CN-M (see inset and Fig. S5), indicating that they have high oxidation-reduction stability. In contrast, two obvious redox peaks caused by oxidation of Ag to Ag_2O and reduction of Ag_2O to Ag are observed at about 0.31 V and -0.005 V, respectively [46], confirming that metallic silver exists in the prepared CN-M-A. Fig. 5(b) depicts the Raman spectra. The characteristic peaks of the C–N extended network at 472, 707, 752, 978, 1234, and 1312 cm^{-1} are consistent with those obtained from pristine CN in literature [10]. Furthermore, the intensity of all Raman peaks in CN-A is higher than that of the CN. This enhancement originates from charge transfer between metallic silver and CN molecules, corroborating the existence of the former [45]. However, the intensity of Raman peaks is depressed notably after introducing MoS_2 nanosheets. The characteristic peaks at 383 and 408 cm^{-1} ascribed to the in-plane E_{2g} and out-of-plane A_{1g} modes of MoS_2 [10], respectively, are not observed. The results imply the existence of strong photoluminescence effect due to the hybridization between metallic Ag and MoS_2 nanosheets in CN-M-A.

The structural information of the samples is also investigated by FTIR spectra and XRD. The FTIR spectra in Figure S6 show typical stretching modes of C–N heterocycles in the $850\text{--}1600\text{ cm}^{-1}$ region, breathing mode of tri-s-triazine units at 809 cm^{-1} , and stretching vibration mode of N–H bond at 3168 cm^{-1} , indicating the presence of a typical CN structure. Fig. 5(c) depicts XRD patterns, which can be indexed to those of pristine CN and MoS_2 nanosheets. The weak peaks at 14.3° and 39.4° originating from the ultrathin MoS_2 nanosheets are in good agreement with a hexagonal structure of MoS_2 (JCPDS No.77-1716) [49]. The salient XRD peaks imply that the exfoliated MoS_2 nanosheets retain good crystallization and well-stacked layered structure without obvious oxidation. The peaks at 12.74° and 27.43° indexed as (100) and (002) peaks of pristine CN correspond to the in-plane structural packing motif of the tri-s-triazine units with the distance of 0.694 nm and interlayer stacking of aromatic segments with a distance of 0.324 nm in the conjugated aromatic system, respectively. Compared to pristine CN, the (100) peak at 12.74° almost disappears from CN-M-A and CN-A, suggesting that those samples possess a layered structure with a small size, which is in good agreement with the result of TEM observations. The processing temperature for Ag reduction in this work is 550°C , which is much higher than the crystallization temperature of Ag. Hence, the absence of Ag peaks in the XRD patterns indicates that the metallic silver is stable and highly dispersed in the nitrogen pots which are filled with six nitrogen lone-pair

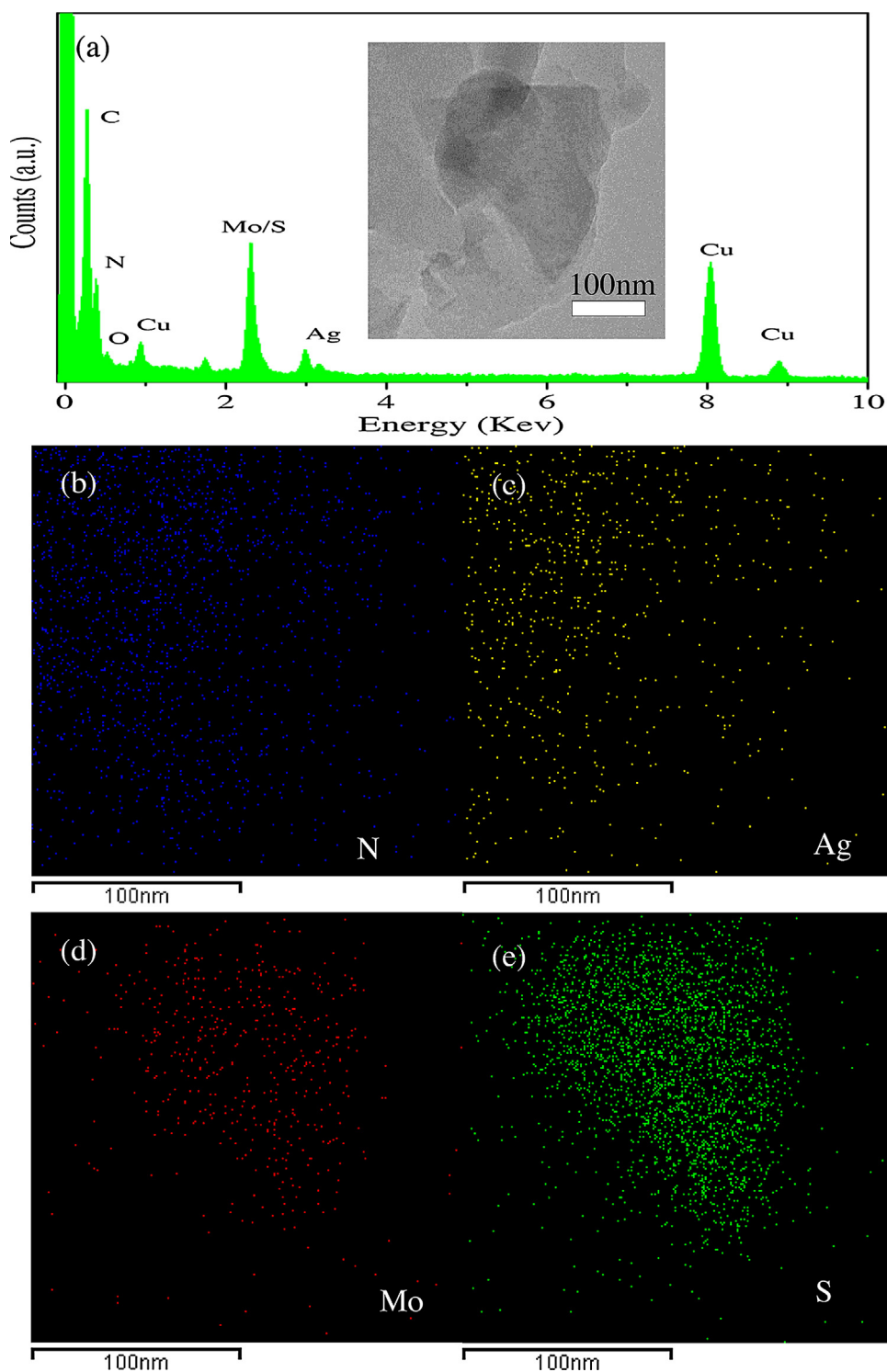


Fig. 4. EDS spectra (a) and corresponding element mappings (b–f) besides carbon of the scanning TEM area shown in the inset obtained from CN–M–A.

electrons in the electron-rich CN structure. The results are similar with those reported in transition metal modified CN samples [14,15].

The surface electronic states and chemical composition of the prepared CN–M–A are further assessed by XPS. The survey XPS spectrum in Fig. S7a discloses the presence of C, N, Mo, S, and Ag with a C/N atomic ratio of 0.79 which is close to the theoretical value for C_3N_4 (0.75). The high-resolution C 1s spectrum in Fig. 6(a) displays four deconvoluted peaks at 284.8, 285.8, 288.3, and 288.9 eV.

The peak at 284.8 eV corresponds to graphitic carbon, and that at 285.8 eV is characteristic of C–N groups, which are usually observed from carbon nitrides. The peak at 288.3 eV corresponds to C=N coordination, whereas the peak at 288.9 eV is identified as sp^2 -hybridized C in the N–C=N coordination [10]. The asymmetrical N1s XPS signal in Fig. 6(b) can be fitted with three peaks at 398.83, 399.87, and 401.06 eV. The main N 1s peak at 398.83 eV corresponds to sp^2 -hybridized aromatic N bound to C atoms (C=N–C) and that at 399.87 eV is assigned to tertiary N bonded to C atoms

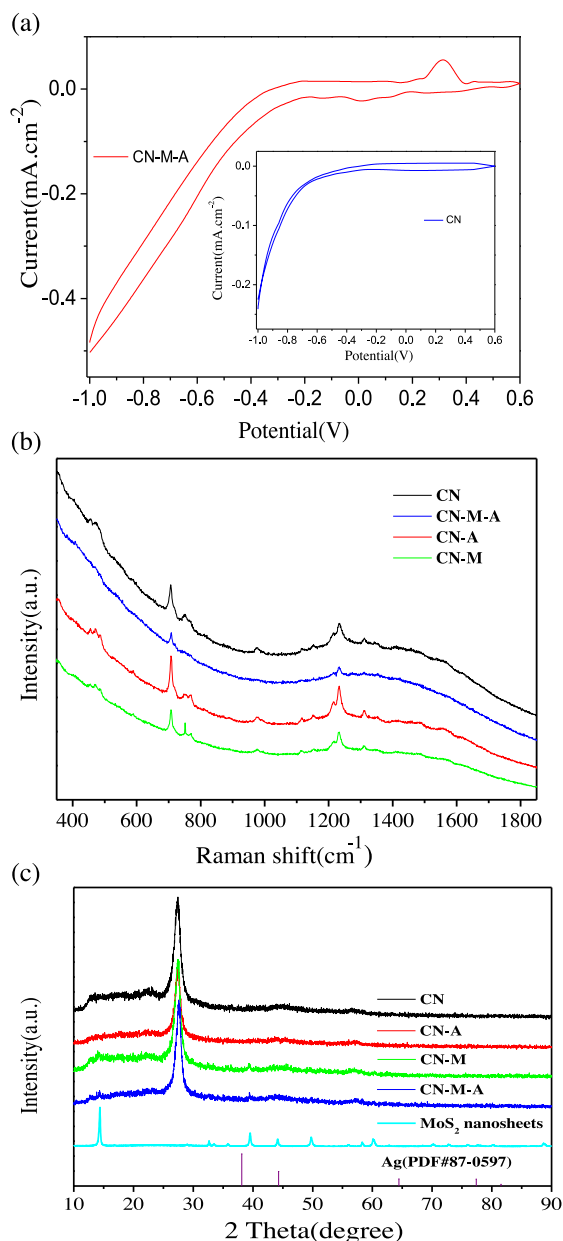


Fig. 5. (a) CV curve of the CN-M-A photoelectrode. The inset shows the CV curve of the CN photoelectrode; (b) and (c) Raman spectra and XRD patterns of CN, CN-A, CN-M, and CN-M-A.

in the form of N-(C)₃ [10]. The peak at 401.06 eV derives from the N-H structure and the weak one at 404.6 eV is attributed to p excitation. The XPS results of carbon and nitrogen elements reveal that chemical structure of pristine CN in the prepared CN-M-A composites of in-planar connected tri-s-triazine subunits, suggesting that the molecular structure of pristine CN is mostly unaltered after the modification with a small amount of metallic silver and MoS₂ nanosheets. Fig. 6(c) shows high-resolution Ag3d XPS spectrum, which can be fitted well with two spin-orbit doublets using Gaussian fitting method. The peaks at 368.38 and 374.43 eV correspond to the binding energies of Ag3d_{5/2} and Ag3d_{3/2}, respectively. The spin energy separation is 6.05 eV, indicating that the silver in CN-M-A has a metallic nature [48]. As shown in Fig. 6(d), two peaks for Mo 3d are observed at 229.2 and 232.1 eV, which are assigned to Mo 3d_{5/2} and Mo 3d_{3/2}, respectively. These values agree well with the literature and are known to be due to Mo⁴⁺ species in the form

of pure MoS₂ [27]. The weak S 2s bands at 225.9 eV are also present, indicating the dominance of Mo⁴⁺ and S²⁻ and further confirmed by the S 2p core spectra in Fig. S7b. The small doublet sub-bands for Mo 3d at 232.8 and 235.2 eV are observed, disclosing the presence of Mo⁶⁺ presumably because of the formation of a minute amount of surface oxide (MoO₃). In addition, the binding energy of Mo 3d is smaller than that reported previously [27], thereby suggesting strong electron coupling between MoS₂ nanosheets and conjugated CN layers [9]. Based on aforementioned results, metallic silver and MoS₂ nanosheets are embedded in CN matrix. Inevitably, nanoscale Mott-Schottky effect exists due to *in situ* coupling between metallic silver and CN nanosheets in such ternary photocatalyst [46]. In addition, intimate contact between MoS₂ and CN nanosheets modified by metallic silver forms 2D CN/MoS₂ heterojunction. The ternary heterojunction photocatalyst embedded with nanoscale Mott-Schottky effect is expected to favor the charge separation and transfer of photogenerated electron-hole pairs, thereby enhancing photocatalytic efficiency. It should be pointed out that the MoO₃ on the surface likely lead to the formation of CN/MoO₃ or MoS₂/MoO₃ heterojunction. However, due to its minor content, possible effect of MoO₃ is neglected in the following discussions.

The optical properties of the samples are studied by UV-vis absorption spectroscopy and PL. As shown in Fig. 7(a), a typical semiconductor absorption in the region of 200–450 nm can be observed from pristine CN, which originates from charge transfer response from the VB populated by N 2p orbitals to the CB formed by C 2p orbitals in pristine CN. The bandgap of the prepared CN estimated with Kubelka-Munk function is 2.72 eV (see the inset of Fig. 7(a)), which is consistent with that reported previously [10]. The absorption peak caused by localized surface plasmon resonance effect of Ag nanocrystals at >450 nm is not observed [46], further confirming that the doped metallic silver is ultra-small. The optical bandgap of CN-A shifts to a lower energy and its light harvesting ability at wavelengths between 400 and 700 nm increases, reflecting host-guest interaction between CN and metallic silver. In contrast, significant intensity enhancement in visible absorption region from 500 to 750 nm and slight blue-shift of absorption edge are observed from CN-M. The former is attributed to smaller bandgap of MoS₂ nanosheets, while the latter is rendered by light scattering effects of nanosheet structure [10,33,38]. However, slightly smaller absorption intensity and obvious red-shift of absorption edge are observed from CN-M-A compared to CN-M, implying hybridization effect between metallic silver and MoS₂ nanosheets on electronic structure and light harvesting ability of ternary photocatalyst. Fig. 7(b) shows PL spectra of the obtained CN, CN-A, CN-M and CN-M-A. The emission peak at about 450 nm is attributed to band-band PL with light energy approximately equal to the band-gap energy of pristine CN. Quenching of PL intensity from CN-A and CN-M was observed, indicating that the photo-generated electrons and holes have better separation due to the introduction of metallic silver or MoS₂ nanosheets [10]. In general, under visible light irradiation, electrons in excited state are transported from the conduction band of pristine CN to Ag or MoS₂ nanosheets owing to Mott-Schottky effect at g-C₃N₄/Ag interface or 2D p-n heterojunction at g-C₃N₄/MoS₂ interface, thereby preventing direct recombination of electrons and holes. Actually, the deep reason for this phenomenon is still unclear and needs further research by time-resolved PL since radiative recombination and non-radiative recombination simultaneously competitive each other, and increased non-radiative recombination benefits the separation of photogenerated electrons and holes with the quenching of PL intensity. Compared to CN-M, PL intensity from CN-M-A is further depressed. The results indicate that the separation efficiency of photogenerated electrons and holes in CN-M-A becomes even more efficient, implying the existence of synergistic interaction between embedded Mott-Schottky effect and 2D

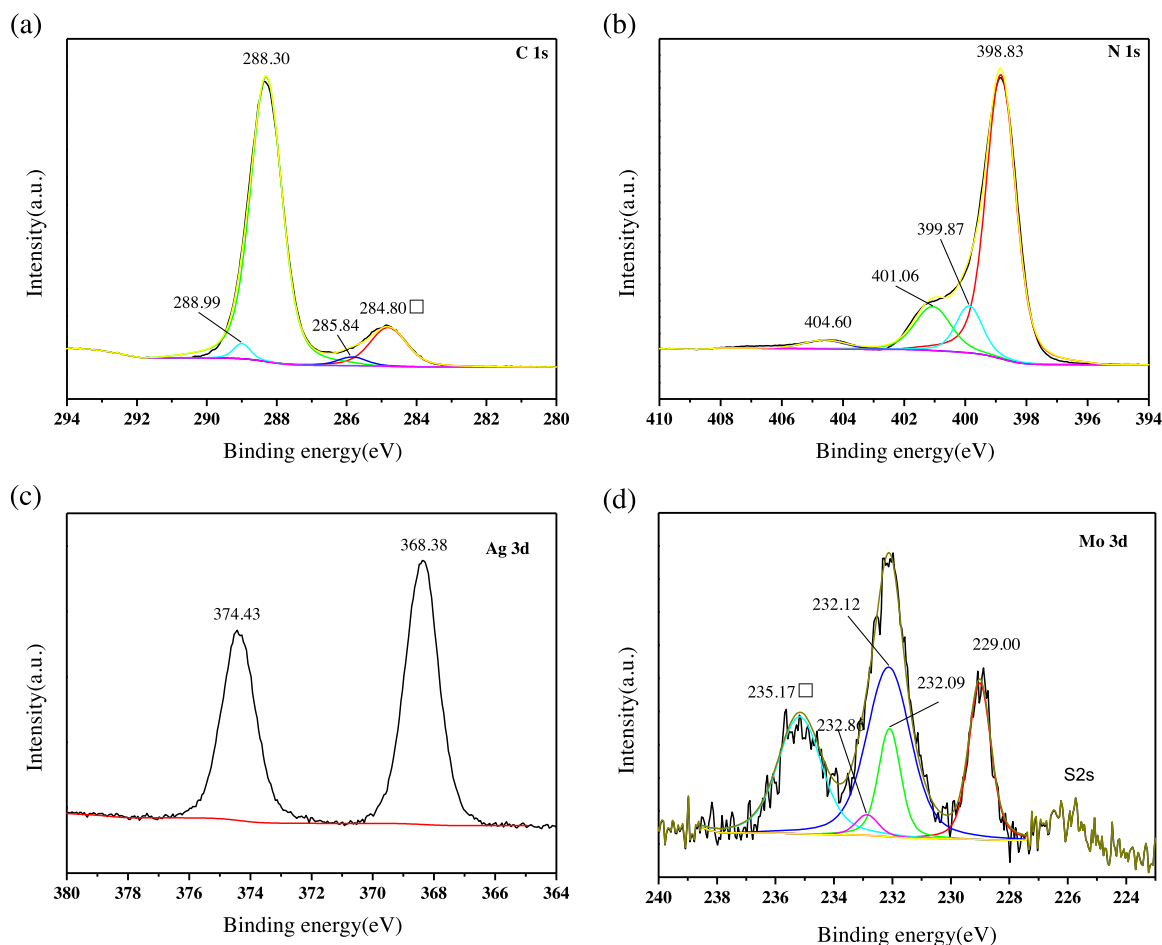


Fig. 6. (a–d) High-resolution C 1s, N 1s, Ag 3d and Mo 3d XPS spectra of the CN–M–A ternary nanocomposite.

g-C₃N₄/MoS₂ heterojunction. In particular, based on the results of nitrogen gas porosimetry, UV–vis absorption and PL spectra, excellent photocatalytic performance from the CN–M–A ternary photocatalyst discussed later is not mainly attributed to improved light harvesting originating from larger surface area, but instead better separation efficiency of photogenerated electrons and holes rendered by interface engineering in heterojunction.

To understand the role of metallic silver and MoS₂ nanosheets in photoelectrochemical performance, transient photocurrents of the samples are measured during repeated five ON/OFF illumination cycles at 0.5 V (see Fig. 7(c)). Fast and uniform photocurrent responses to each switch-on and switch-off event can be observed for all samples. The results are reproducible, implying that most of the photogenerated electrons are transported to back contact across the samples to produce photocurrent under visible light irradiation. A photocurrent density of 1.01 $\mu\text{A cm}^{-2}$ is observed from the CN electrode under visible light irradiation, corresponding to the photo excitation of polymeric semiconductor. The transient photocurrent density of the CN–M electrode increases to 1.58 $\mu\text{A cm}^{-2}$. The result indicates the constructive effect of the MoS₂ nanosheets in suppressing charge recombination owing to 2D heterojunction built between CN and MoS₂ nanosheets. This enables the photogenerated electrons to be transferred to MoS₂ nanosheets to enhance separation efficiency. A higher photocurrent density of 2.17 $\mu\text{A cm}^{-2}$ can be observed from the CN–A electrode due to enhanced light harvesting from unique geometry of thin nanosheet and efficient separation of photogenerated electron–hole pairs from Mott–Schottky effect at g-C₃N₄/Ag

interface. The highest transient photocurrent density reaching 3.12 $\mu\text{A cm}^{-2}$ can be obtained from the CN–M–A electrode, which is about 3 times that of the CN electrode. Assuming that the number of electron–hole pairs generated from all electrodes is comparable, the enhanced photocurrent density from CN–M–A is more than those from CN–A, CN–M, and even simple addition of CN–A and CN–M. The results illustrate synergistic effect between metallic silver and MoS₂ nanosheets on the separation of photo-generated electron–hole pairs. The coupling between lone electron pair from the outer layer of N component in pristine CN and the outer-most 5S sublayer of metallic Ag enhances the conductivity of CN nanosheets to accelerate electron transfer between CN and MoS₂ [46]. More importantly, the Mott–Schottky effect between CN nanosheets and metallic silver bends energy band of the latter upwards, thereby promoting the separation of photogenerated electron–hole pairs at the CN/MoS₂ heterojunction due to enhanced interfacial electric field [42,43,46]. Consequently, direct recombination of photogenerated electron–hole pairs in the CN–M–A is depressed notably and the photocurrent density is enhanced greatly. Although the photocurrent density measured from the CN–M–A electrode is still moderate due to the test conditions compared to values in the literatures [6,19,50–52], these results are very encouraging. The enhancement of photocurrent density measured from the CN–M–A electrode is higher than that of the 2D CN/MoS₂ heterojunction (2-fold) [41], and comparable to that of the 2D ternary nanojunction consisting of porous CN nanosheets, nitrogen-doped graphene, and layered MoS₂ (3.06-fold) [10]. It can be viewed as a feasible strategy for the separation

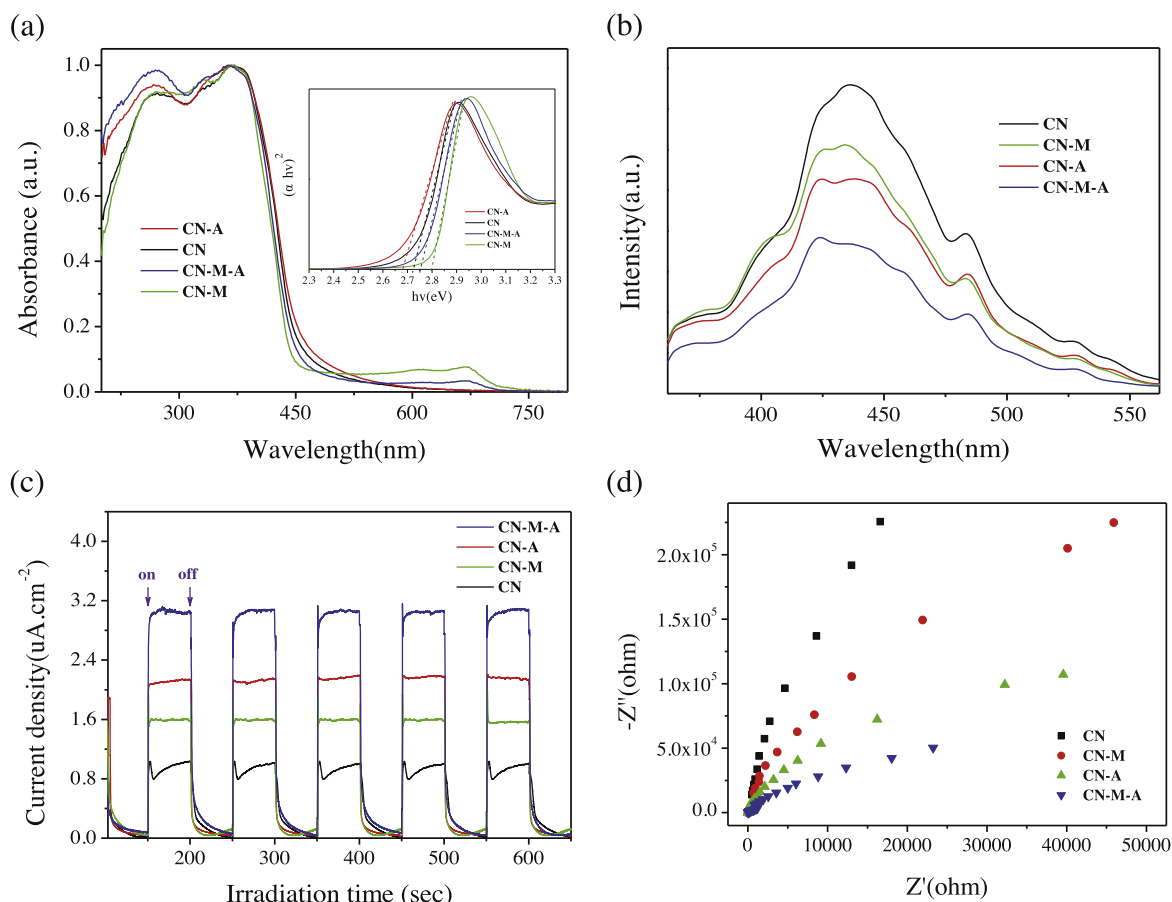


Fig. 7. (a) UV-vis diffuse reflectance spectra of CN, CN-A, CN-M and CN-M-A. The inset shows the corresponding plots of $(\alpha h\nu)^2$ vs. $h\nu$; (b) PL spectra of CN, CN-A, CN-M and CN-M-A excited by 350 nm wavelength at room temperature; (c) Transient photocurrent responses of the CN, CN-M, CN-A and CN-M-A electrodes in 0.5 M Na_2SO_4 aqueous solution under visible light irradiation at 0.5 V vs. Ag/AgCl electrode; (d) EIS Nyquist plots of the CN, CN-M, CN-A and CN-M-A electrodes under visible light irradiation.

and migration of photogenerated electron-hole pairs in CN-based photocatalyst to improve photocatalytic performance considering that the preparation parameters of CN-M-A have not yet been optimized. To gain more insights into charge transport behavior, EIS is conducted on various electrodes (see Fig. 7(d)). In Nyquist diagram, a smaller radius is an indication of an overall smaller charge transfer resistance or, equivalently, a more facile charge transfer process at the electrode/electrolyte interface [53,54]. One can see that the arc radius of the CN-M-A electrode is the smallest one and so it has the smallest charge transfer resistance among four CN-based electrodes. The integration of 2D $\text{g-C}_3\text{N}_4/\text{MoS}_2$ heterojunction with nanoscale Mott-Schottky effect improves shuttling of charges between the electrode and electrolyte, and consequently faster interfacial charge transfer and separation *via* the synergistic interaction among CN, metallic silver, and MoS_2 nanosheets.

In order to demonstrate improved photocatalytic activities of the CN-M-A ternary nanocomposite, we evaluated the photodegradation of RhB as a function of time under visible light irradiation. Prior to light illumination, the reaction mixture was stirred for 30 min in darkness in order to reach adsorption/desorption equilibrium between dye and catalyst. A control experiment was carried out first and almost no degradation of the RhB was observed. As shown in Fig. 8a, the adsorption equilibrium states are reached in 30 min for all materials tested in the darkness. After attaining equilibrium in the absence of light for 1 h, a large amount of RhB molecules are adsorbed on the surface of

CN-A, CN-M, and especially CN-M-A. The enhanced adsorptivity of hybrid photocatalysts prefigures improved performance in the photodegradation of RhB. The ternary CN-M-A exhibits the highest photocatalytic activity for the degradation of RhB and almost complete removal of RhB ($\sim 98.6\%$) is observed after irradiation for 60 min. It is better than those of CN (65.8%), CN-A (83.2%), and CN-M (79.5%). Assuming that photocatalytic reaction follows a pseudo-first-order reaction (Fig. 8b), the kinetic constant of CN-M-A (0.06662 min^{-1}) is about 3.83, 2.36 and 2.63 times higher than those of CN (0.01737 min^{-1}), CN-A (0.02815 min^{-1}) and CN-M (0.02530 min^{-1}), respectively, further confirming enhanced photocatalytic capability of CN-M-A. The improved RhB degradation rate of CN-M-A is even higher than that of simple addition of CN-A and CN-M, implying that the synergistic effect exists between metallic Ag and MoS_2 nanosheets, which plays an important role in preventing direct recombination of electron-hole pairs. Consequently separation of photogenerated electron-hole pairs in ternary CN-M-A is expedited and so more holes and electrons participate in the photocatalytic reactions instead of recombination. The stability of the CN-M-A is investigated by recycling the photocatalyst for RhB degradation under visible light irradiation. As shown in Figs. 8(c) and 9(a), the photocatalytic activity does not exhibit any significant loss and the crystal structure keeps unchanged after five consecutive recycling runs, indicating that ternary CN-M-A possesses excellent photocatalytic stability. To elucidate photocatalytic mechanism, main reactive species in the photocatalytic process of RhB over CN-M-A are monitored by

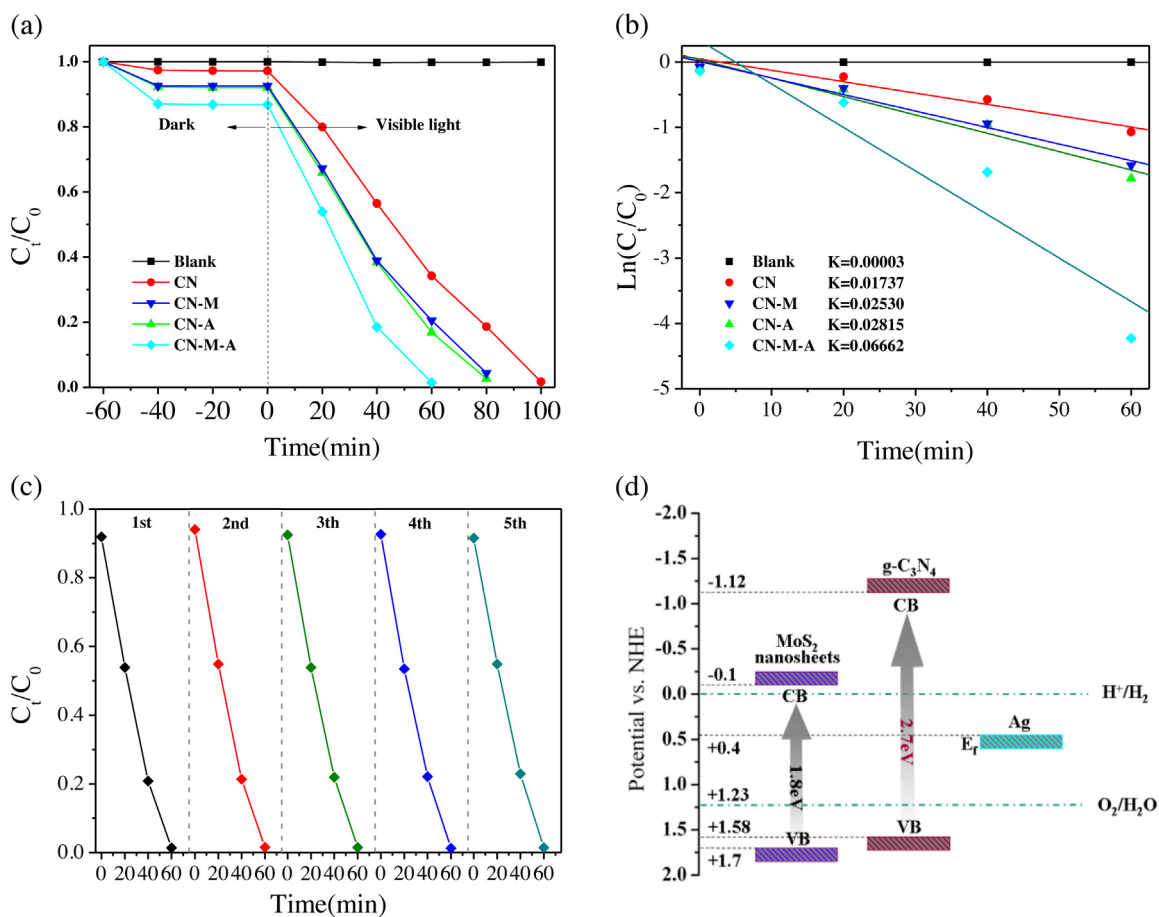


Fig. 8. (a) Photocatalytic degradation rates of the RhB under visible light irradiation ($\lambda > 400$ nm, $C_0 = 10 \text{ mg L}^{-1}$, $I_0 = 100 \text{ mW cm}^{-2}$) for CN, CN-A, CN-M and CN-M-A; (b) corresponding $\ln(C_t/C_0)$ of the RhB vs. time for different photocatalytic materials under visible light irradiation. (c) Cycling runs for the photocatalytic degradation of the RhB in the presence of CN-M-A under visible light irradiation. (d) Schematic energy level diagrams of CN nanosheets, metallic silver and MoS_2 nanosheets in comparison with the potentials of water reduction and oxidation.

radical trapping experiments. N_2 purging, tert-butyl alcohol (t-BuOH) and EDTA-2Na are used as superoxide ($\cdot\text{O}_2^-$), hydroxyl ($\cdot\text{OH}$) and hole (h^+) radical scavenger, respectively. As shown in Fig. 9(b), the photocatalytic activity of CN-M-A is suppressed by the addition of radical scavengers. Because the VB position of pristine CN (1.57 eV vs. NHE) is more negative than that of $\cdot\text{OH}/\text{OH}^-$ (1.99 eV vs. NHE), the holes may react with the RhB directly. The $\cdot\text{OH}$ radicals usually originate from the reaction of photogenerated electrons with adsorbed O_2 [10]. The radical trapping results reveal that the $\cdot\text{O}_2^-$ radicals are primary active species in the CN-M-A ternary nanocomposite, in which both $\cdot\text{OH}$ and holes are involved in the photocatalytic reaction of RhB.

The aforementioned results demonstrate outstanding photoelectrochemical performance and photocatalytic activity of ternary CN-M-A nanocomposite as a genuine heterogeneous visible-light-driven photocatalyst. Based on the band gap of pristine CN, metallic silver, and MoS_2 nanosheets, a tentative electron-hole separation and transport process (see Fig. S8) for ternary CN-M-A system under visible light irradiation is proposed. According to the reported energy level diagram (see Fig. 8(d)), the band gap of MoS_2 nanosheets increases due to quantum size effect, and the conduction-band and valence-band potentials are estimated to be -0.1 and 1.7 eV [10], which are more positive than those of pristine CN. Under visible light irradiation, electrons are promoted from the valence bands of CN and MoS_2 nanosheets to their respective conduction bands to simultaneously create holes in the valence

bands. Owing to band alignment and potential difference [6,8,55], photogenerated electrons in the conduction band of CN can be transferred to the conduction band of MoS_2 . Simultaneously, the holes at the valence band of MoS_2 migrate to that of CN due to the internal electric field formed by space charge layer between 2D CN/ MoS_2 interface. On the other hand, since the Fermi level of Ag at 0.4 eV is more positive than the conduction band potential of pristine CN, photogenerated electron can be envisioned to transfer from the conduction band of CN to metallic Ag, resulting in a positively charged region and a negatively charged particle to minimize the recombination of photogenerated electron-hole pairs due to the Mott-Schottky effect. Moreover, modulated energy band of CN nanosheets due to the modification from metallic silver facilitates the separation and transport of photogenerated electrons and holes at the interface of 2D CN/ MoS_2 heterojunction. As a result, the photo-excited electrons are mainly collected by metallic Ag and MoS_2 nanosheets, where the photoreduction reactions occur [9], and the holes by CN and are finally consumed by photooxidation reactions. This leads to the activation of two substrates toward electron-rich and electron-deficient intermediates respectively, similar to the frustrated Lewis pairs [43], and hence, the recombination process of the electron-hole pairs is hindered and effective charge separation is achieved to facilitate photocatalytic reaction. The reactions by holes in CN and highly active $\cdot\text{OH}$ groups generated from the photoreduction reactions of oxygen by electrons collected on the surface of MoS_2 nanosheets and metallic Ag make the RhB decompose into CO_2 , H_2O or other

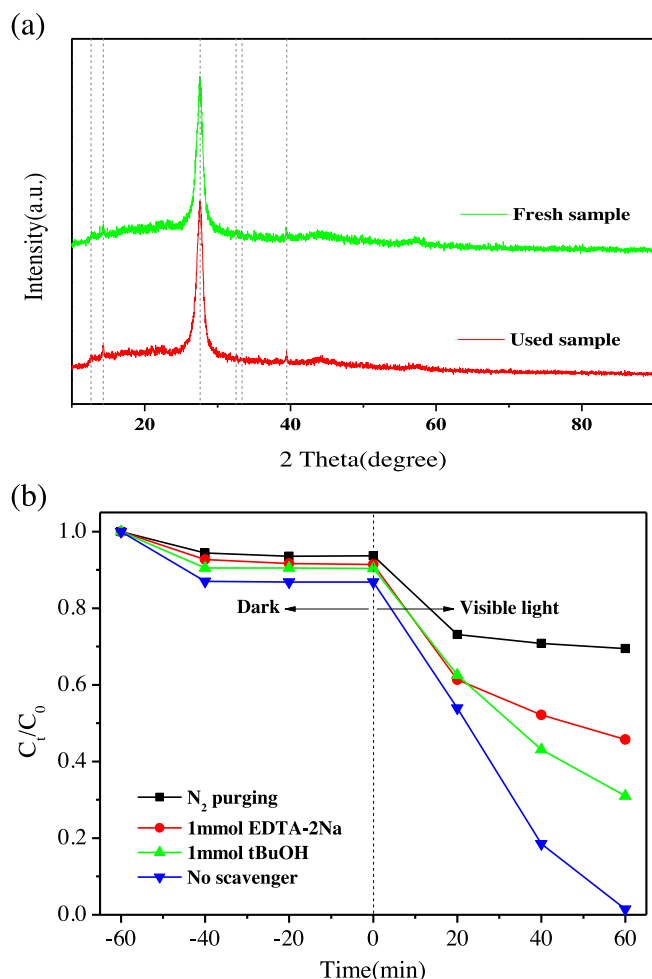


Fig. 9. (a) XRD patterns of CN-M-A before and after five cycling runs for the photocatalytic degradation of RhB under visible light irradiation. (b) Kinetic curves for the photocatalytic degradation of RhB over CN-M-A with the addition of superoxide ($\text{O}_2^{\cdot-}$), hole and hydroxyl radical scavenger under visible light irradiation.

intermediates, consequently producing enhanced photocatalytic activity of the CN-M-A ternary nanocomposite.

4. Conclusions

In summary, we have demonstrated the use of AgNO_3 as a multifunctional modifier during thermal polymerization of melamine to *in situ* control the texture, surface chemistry, light-harvesting ability and semiconductor properties of the prepared ternary mesoporous photocatalyst consisting of CN nanosheets, metallic silver and MoS_2 nanosheets. In this ternary nanocomposite, *in situ* coupling between metallic silver and CN nanosheets produces nanoscale Mott–Schottky effect, provides an effective channel for charge separation and transfer, and tunes the energy band of the latter. More importantly, modulated energy band of the CN nanosheets synergistically facilitates charge separation and transfer at the interface of 2D CN/ MoS_2 heterojunction. Consequently, the ternary photocatalyst exhibits even more efficient separation and transfer of photogenerated electron–hole pairs to improve photoelectrochemical performance and photocatalytic activity under simulated sunlight irradiation compared to other reference materials. Our results provide insights to the design and large-scale production of semiconductor photocatalysts by interface engineering of the heterojunction and *in situ* coupling with a co-catalyst.

Acknowledgments

This work was financially supported by the Grants from National Natural Science Foundation of China (Nos. 51272220, 11374252, 11474242 and 51472209), the Program for Changjiang Scholars and Innovative Research Team in University (IRT13093), and Guangdong-Hong Kong Technology Cooperation Funding Scheme (TCFS) GHP/015/12SZ.

Appendix A. Supplementary data

Supplementary data associated with this article can be found, in the online version, at <http://dx.doi.org/10.1016/j.apcatb.2014.08.023>.

References

- [1] X. Chen, S. Shen, L. Guo, S.S. Mao, Chem. Rev. 110 (2010) 6503–6570.
- [2] Q. Xiang, J. Yu, M. Jaroniec, Chem. Soc. Rev. 41 (2012) 782–796.
- [3] Y. Qu, X. Duan, Chem. Soc. Rev. 42 (2013) 2568–2580.
- [4] J. Yang, D. Wang, H. Han, C. Li, Acc. Chem. Res. 46 (2013) 1900–1909.
- [5] X. Wang, K. Maeda, A. Thomas, K. Takanabe, G. Xin, J.M. Carlsson, K. Domen, M.A. Antonietti, Nat. Mater. 8 (2009) 76–80.
- [6] Y. Wang, X. Wang, M. Antonietti, Angew. Chem. Int. Ed. 51 (2012) 68–89.
- [7] Y. Zheng, J. Liu, J. Liang, M. Jaroniec, S.Z. Qiao, Energy Environ. Sci. 5 (2012) 3731–3717.
- [8] J. Zhang, M. Zhang, R.Q. Sun, X. Wang, Angew. Chem. Int. Ed. 124 (2012) 10292–10296.
- [9] Y. Hou, A.B. Laursen, J. Zhang, G. Zhang, Y. Zhu, X. Wang, S. Dahl, I. Chorkendorff, Angew. Chem. Int. Ed. 52 (2013) 3621–3625.
- [10] Y. Hou, Z. Wen, S. Cui, X. Guo, J. Chen, Adv. Mater. 25 (2013) 6291–6297.
- [11] Z. Lin, X. Wang, Angew. Chem. Int. Ed. 52 (2013) 1735–1738.
- [12] S. Yang, Y. Gong, J. Zhang, L. Zhan, L. Ma, Z. Fang, R. Vajtai, X. Wang, P.M. Ajayan, Adv. Mater. 25 (2013) 2452–2456.
- [13] X. Chen, J. Zhang, X. Fu, M. Antonietti, X. Wang, J. Am. Chem. Soc. 131 (2009) 11658–11659.
- [14] Z. Ding, X. Chen, M. Antonietti, X. Wang, ChemSusChem 4 (2011) 274–281.
- [15] X. Wang, X. Chen, A. Thomas, X. Fu, M. Antonietti, Adv. Mater. 21 (2009) 1609–1612.
- [16] G. Liu, P. Niu, C. Sun, S.C. Smith, Z. Chen, G.Q. Lu, H.M. Cheng, J. Am. Chem. Soc. 132 (2010) 11642–11648.
- [17] Y. Wang, J. Zhang, X. Wang, M. Antonietti, H. Li, Angew. Chem. Int. Ed. 49 (2010) 3356–3359.
- [18] G. Zhang, M. Zhang, X. Ye, X. Qiu, S. Lin, X. Wang, Adv. Mater. 26 (2013) 805–809.
- [19] Y. Zhang, T. Mori, J. Ye, M. Antonietti, J. Am. Chem. Soc. 132 (2010) 6294–6295.
- [20] A. Kubacka, M. Fernández-García, G. Colón, Chem. Rev. 112 (2012) 1555–1614.
- [21] H. Tong, S. Ouyang, Y. Bi, N. Umezawa, M. Oshikiri, J. Ye, Adv. Mater. 24 (2012) 229–251.
- [22] L. Ge, C. Han, J. Liu, Appl. Catal. B-Environ. 108–109 (2011) 100–107.
- [23] S. Kumar, T. Surendar, A. Baruah, V. Shanker, J. Mater. Chem. A 1 (2013) 5333–5340.
- [24] C. Pan, J. Xu, Y. Wang, D. Li, Y. Zhu, Adv. Funct. Mater. 22 (2012) 1518–1524.
- [25] H. Xu, J. Yan, Y. Xu, Y. Song, H. Li, J. Xia, C. Huang, H. Wan, Appl. Catal. B-Environ. 129 (2013) 182–193.
- [26] Q.H. Wang, K. Kalantar-Zadeh, A. Kis, J.N. Coleman, M.S. Strano, Nat. Nanotechnol. 7 (2012) 699–712.
- [27] J. Kibsgaard, Z. Chen, B.N. Reinecke, T.F. Jaramillo, Nat. Mater. 11 (2012) 963–969.
- [28] L. Ge, C. Han, Appl. Catal. B-Environ. 117 (2012) 268–274.
- [29] X.H. Li, J.S. Chen, X. Wang, J. Sun, M. Antonietti, J. Am. Chem. Soc. 133 (2011) 8074–8077.
- [30] Y. Li, H. Zhang, P. Liu, D. Wang, Y. Li, H. Zhao, Small 9 (2013) 3336–3344.
- [31] J. Liang, Y. Zheng, J. Chen, J. Liu, D. Hulicova Jurcakova, M. Jaroniec, S.Z. Qiao, Angew. Chem. Int. Ed. 51 (2012) 3892–3896.
- [32] S. Yang, X. Feng, X. Wang, K. Müllen, Angew. Chem. Int. Ed. 50 (2011) 5339–5343.
- [33] J.S. Jun, E.Z. Lee, X. Wang, W.H. Hong, G.D. Stucky, A. Thomas, Adv. Funct. Mater. 23 (2013) 3661–3667.
- [34] J. Zhang, F. Guo, X. Wang, Adv. Funct. Mater. 23 (2013) 3008–3014.
- [35] Y. Zhang, J. Liu, G. Wu, W. Chen, Nanoscale 4 (2012) 5300–5303.
- [36] Y. Zhang, Z. Schniepp, J. Cao, S. Ouyang, Y. Li, J. Ye, S. Liu, Sci. Rep. 3 (2013) 2163.
- [37] S.W. Bian, Z. Ma, W.G. Song, J. Phys. Chem. C 113 (2009) 8668–8672.
- [38] X.H. Li, J. Zhang, X. Chen, A. Fischer, A. Thomas, M. Antonietti, X. Wang, Chem. Mater. 23 (2011) 4344–4348.
- [39] Z. Zhang, J.T. Yates Jr., Chem. Rev. 112 (2012) 5520–5551.
- [40] F. Meng, J. Li, S.K. Cushing, M. Zhi, N. Wu, J. Am. Chem. Soc. 135 (2013) 10286–10289.
- [41] Q. Li, N. Zhang, Y. Yang, G.Z. Wang, D.H.L. Ng, Langmuir 30 (2014) 8965–8972.
- [42] X.H. Li, M. Antonietti, Chem. Soc. Rev. 42 (2013) 6593–6604.
- [43] X.H. Li, M. Baar, S. Blechert, M. Antonietti, Sci. Rep. 3 (2013) 1743.
- [44] L. Ge, C. Han, J. Liu, Y. Li, Appl. Catal. A-Gen. 409 (2011) 215–222.

- [45] X. Bai, R. Zong, C. Li, D. Liu, Y. Liu, Y. Zhu, *Appl. Catal. B-Environ.* 147 (2013) 82–91.
- [46] Y. Bu, Z. Chen, W. Li, *Appl. Catal. B-Environ.* 144 (2013) 622–630.
- [47] Y. Di, X. Wang, A. Thomas, M. Antonietti, *ChemCatChem* 2 (2010) 834–838.
- [48] Y. Yang, Y. Guo, F. Liu, X. Yuan, Y. Guo, S. Zhang, W. Guo, M. Huo, *Appl. Catal. B-Environ.* 142 (2013) 828–837.
- [49] Y. Liu, L. Ren, X. Qi, L. Yang, G. Hao, J. Li, X. Wei, J. Zhong, *J. Alloys Compd.* 571 (2013) 37–42.
- [50] J. Zhang, J. Sun, K. Maeda, K. Domen, P. Liu, M. Antonietti, X. Fu, X. Wang, *Energy Environ. Sci.* 4 (2011) 675–678.
- [51] Y. Zhang, T. Mori, L. Niu, J. Ye, *Energy Environ. Sci.* 4 (2011) 4512–4517.
- [52] Y. Zhang, A. Thomas, M. Antonietti, X. Wang, *J. Am. Chem. Soc.* 131 (2008) 50–51.
- [53] Y. Hou, F. Zuo, A. Dagg, P.A. Feng, *Angew. Chem.* 125 (2013) 1286–1290.
- [54] S. Yu, L. Yang, Y. Tian, P. Yang, F. Jiang, S. Hu, X. Wei, J. Zhong, *J. Mater. Chem. A* 1 (2013) 12750–12758.
- [55] Q. Xiang, J. Yu, M. Jaroniec, *J. Am. Chem. Soc.* 134 (2012) 6575–6578.